Temperature-dependent absorption and emission of potassium double tungstates with high ytterbium content

YEAN-SHENG YONG,[1,*] SHANMUGAM ARAVAZHI,[2] SERGIO A. VÁZQUEZ-CÓRDOVA,[1] JOAN J. CARJAVAL,[3] FRANCESC DÍAZ,[3] JENNIFER L. HEREK,[1] SONIA M. GARCÍA-BLANCO,[1] AND MARKUS POLLNAU[2,4]

[1]Optical Sciences Group, MESA+ Institute for Nanotechnology, University of Twente, P.O. Box 217, 7500 AE Enschede, Netherlands
[2]Integrated Optical Microsystems Group, MESA+ Institute for Nanotechnology, University of Twente, P.O. Box 217, 7500 AE Enschede, Netherlands
[3]Física i Cristal·lografia de Materials i Nanomaterials (FiCMA-FiCNA) and EMaS, Universitat Rovira i Virgili (URV), Campus Sescelades, c/Marcel·lí Domingo s/n, E-43007 Tarragona, Spain
[4]Department of Materials and Nano Physics, School of Information and Communication Technology, KTH–Royal Institute of Technology, Electrum 229, Isafjordsgatan 22–24, 16440 Kista, Sweden
*y.s.yong@utwente.nl

Abstract: We study the spectroscopic properties of thin films of potassium ytterbium gadolinium double tungstates, $KYb_{0.57}Gd_{0.43}(WO_4)_2$, and potassium ytterbium lutetium double tungstates, $KYb_{0.76}Lu_{0.24}(WO_4)_2$, specifically at the central absorption line near 981 nm wavelength, which is important for amplifiers and lasers. The absorption cross-section of both thin films is found to be similar to those of bulk potassium rare-earth double tungstates, suggesting that the crystalline layers retain their spectroscopic properties albeit having >50 at.% Yb^{3+} concentration. The influence of sample temperature is investigated and found to substantially affect the measured absorption cross-section. Since amplifiers and lasers typically operate above room temperature due to pump-induced heating, the temperature dependence of the peak-absorption cross-section of the $KYb_{0.57}Gd_{0.43}(WO_4)_2$ is evaluated for the sample being heated from 20 °C to 170 °C, resulting in a measured reduction of peak-absorption cross-section at the transitions near 933 nm and 981 nm by ~40% and ~52%, respectively. It is shown that two effects, the change of Stark-level population and linewidth broadening due to intra-manifold relaxation induced by temperature-dependent electron-phonon interaction, contribute to the observed behavior. The effective emission cross-sections versus temperature have been calculated. Luminescence-decay measurements show no significant dependence of the luminescence lifetime on temperature.

References and links

1. N. V. Kuleshov, A. A. Lagatsky, A. V. Podlipensky, V. P. Mikhailov, and G. Huber, "Pulsed laser operation of Yb-doped KY(WO₄)₂ and KGd(WO₄)₂," Opt. Lett. **22**(17), 1317–1319 (1997).
2. X. Mateos, M. C. Pujol, F. Guell, M. Galan, R. M. Sole, J. Gavalda, M. Aguilo, J. Massons, and F. Diaz, "Erbium spectroscopy and 1.5-μm emission in KGd(WO₄)₂: Er,Yb single crystals," IEEE J. Quantum Electron. **40**(6), 759–770 (2004).
3. V. Petrov, M. Cinta Pujol, X. Mateos, Ò. Silvestre, S. Rivier, M. Aguiló, R. M. Solé, J. Liu, U. Griebner, and F. Díaz, "Growth and properties of KLu(WO₄)₂, and novel ytterbium and thulium lasers based on this monoclinic crystalline host," Laser Photonics Rev. **1**(2), 179–212 (2007).
4. M. C. Pujol, X. Mateos, R. Solé, J. Massons, J. Gavaldà, X. Solans, F. Díaz, and M. Aguiló, "Structure, crystal growth and physical anisotropy of KYb(WO₄)₂, a new laser matrix," J. Appl. Cryst. **35**(1), 108–112 (2002).
5. P. Klopp, U. Griebner, V. Petrov, X. Mateos, M. A. Bursukova, M. C. Pujol, R. Sole, J. Gavalda, M. Aguilo, F. Güell, J. Massons, T. Kirilov, and F. Diaz, "Laser operation of the new stoichiometric crystal KYb(WO₄)₂," Appl. Phys. B **74**(2), 185–189 (2002).

6. J. Koerner, C. Vorholt, H. Liebetrau, M. Kahle, D. Kloepfel, R. Seifert, J. Hein, and M. C. Kaluza, "Measurement of temperature-dependent absorption and emission spectra of Yb:YAG, Yb:LuAG, and Yb:CaF$_2$ between 20 °C and 200 °C and predictions on their influence on laser performance," J. Opt. Soc. Am. B **29**(9), 2493 (2012).
7. K. Petermann, D. Fagundes-Peters, J. Johannsen, M. Mond, V. Peters, J. J. Romero, S. Kutovoi, J. Speiser, and A. Giesen, "Highly Yb-doped oxides for thin-disc lasers," J. Cryst. Growth **275**(1-2), 135–140 (2005).
8. S. Aravazhi, D. Geskus, K. van Dalfsen, S. A. Vázquez-Córdova, C. Grivas, U. Griebner, S. M. García-Blanco, and M. Pollnau, "Engineering lattice matching, doping level, and optical properties of KY(WO$_4$)$_2$:Gd, Lu, Yb layers for a cladding-side-pumped channel waveguide laser," Appl. Phys. B **111**(3), 433–446 (2013).
9. D. Geskus, S. Aravazhi, S. M. García-Blanco, and M. Pollnau, "Giant optical gain in a rare-earth-ion-doped microstructure," Adv. Mater. **24**(10), OP19–OP22 (2012).
10. D. Geskus, E. H. Bernhardi, K. van Dalfsen, S. Aravazhi, and M. Pollnau, "Highly efficient Yb^{3+}-doped channel waveguide laser at 981 nm," Opt. Express **21**(11), 13773–13778 (2013).
11. O. Silvestre, A. Aznar, R. Solé, M. C. Pujol, F. Díaz, and M. Aguiló, "Lattice mismatch and crystal growth of monoclinic KY$_{1-x}$Yb$_x$(WO$_4$)$_2$/KY(WO$_4$)$_2$ layers by liquid phase epitaxy," J. Phys. Condens. Matter **20**(22), 225004 (2008).
12. F. Balembois, M. Castaing, P. Georges, and T. Georges, "Line competition in an intracavity diode-pumped Yb:KYW laser operating at 981nm," J. Opt. Soc. Am. B **28**(1), 115–122 (2011).
13. B. Jacobsson, "Experimental and theoretical investigation of a volume-Bragg-grating-locked Yb:KYW laser at selected wavelengths," Opt. Express **16**(9), 6443–6454 (2008).
14. M. Pollnau, Y. E. Romanyuk, F. Gardillou, C. N. Borca, U. Griebner, S. Rivier, and V. Petrov, "Double tungstate lasers: From bulk toward on-chip integrated waveguide devices," IEEE J. Sel. Top. Quantum Electron. **13**(3), 661–671 (2007).
15. O. Silvestre, M. C. Pujol, R. Solé, W. Bolaños, J. J. Carvajal, J. Massons, M. Aguiló, and F. Diaz, "Ln^{3+}:KLu(WO$_4$)$_2$/KLu(WO$_4$)$_2$ epitaxial layers: Crystal growth and physical characterisation," Mater. Sci. Eng. B **146**(1-3), 59–65 (2008).
16. M. R. Sharpe, "Stray light in UV-VIS spectrophotometers," Anal. Chem. **56**, 339–356 (1984).
17. D. Luo, J. Zhang, C. Xu, H. Yang, H. Lin, H. Zhu, and D. Tang, "Yb:LuAG laser ceramics: a promising high power laser gain medium," Opt. Mater. Express **2**(10), 1425–1431 (2012).
18. X. Xu, Z. Zhao, P. Song, G. Zhou, J. Xu, and P. Deng, "Structural, thermal, and luminescent properties of Yb-doped Y$_3$Al$_5$O$_{12}$ crystals," J. Opt. Soc. Am. B **21**(3), 543–547 (2004).
19. M. C. Pujol, M. A. Bursukova, F. Güell, X. Mateos, R. Solé, J. Gavaldà, M. Aguiló, J. Massons, F. Díaz, P. Klopp, U. Griebner, and V. Petrov, "Growth, optical characterization, and laser operation of a stoichiometric crystal KYb(WO$_4$)$_2$," Phys. Rev. B **65**(16), 165121 (2002).
20. X. Mateos, R. Solé, J. Gavaldà, M. Aguiló, J. Massons, and F. Díaz, "Crystal growth, optical and spectroscopic characterisation of monoclinic KY(WO$_4$)$_2$ co-doped with Er^{3+} and Yb^{3+}," Opt. Mater. **28**(4), 423–431 (2006).
21. X. Mateos, R. Solé, J. Gavaldà, M. Aguiló, J. Massons, F. Díaz, V. Petrov, and U. Griebner, "Crystal growth, spectroscopic studies and laser operation of Yb^{3+}-doped potassium lutetium tungstate," Opt. Mater. **28**(5), 519–523 (2006).
22. B. E. A. Saleh and M. C. Teich, *Fundamentals of Photonics*, 2nd ed. (Wiley-Interscience, 2007), Chap. 13.
23. M. Eichhorn and M. Pollnau, "Spectroscopic foundations of lasers: spontaneous emission into a resonator mode," IEEE J. Sel. Top. Quantum Electron. **21**(1), 900216 (2015).
24. S. A. Payne, L. L. Chase, L. K. Smith, W. L. Kway, and W. F. Krupke, "Infrared cross-section measurement for crystals doped with Er^{3+}, Tm^{3+}, and Ho^{3+}," IEEE J. Quantum Electron. **28**(11), 2619–2630 (1992).
25. H. Kühn, S. T. Fredrich-Thornton, C. Kränkel, R. Peters, and K. Petermann, "Model for the calculation of radiation trapping and description of the pinhole method," Opt. Lett. **32**(13), 1908–1910 (2007).
26. G. G. Demirkhanyan, H. G. Demirkhanyan, E. P. Kokanyan, R. B. Kostanyan, J. B. Gruber, K. L. Nash, and D. K. Sardar, "Phonon effects on zero-phonon transitions between Stark levels in NaBi(WO$_4$)$_2$:Yb^{3+}," J. Appl. Phys. **105**(6), 063106 (2009).
27. G. G. Demirkhanyan and R. B. Kostanyan, "Temperature dependence of spectral-line intensities in YAG:Yb^{3+}," Laser Phys. **18**(2), 104–111 (2011).
28. T. Y. Fan, D. J. Ripin, R. L. Aggarwal, J. R. Ochoa, B. Chann, M. Tilleman, and J. Spitzberg, "Cryogenic Yb^{3+}-doped solid-state lasers," IEEE J. Sel. Top. Quantum Electron. **13**(3), 448–459 (2007).
29. R. L. Aggarwal, D. J. Ripin, J. R. Ochoa, and T. Y. Fan, "Measurement of thermo-optic properties of Y$_3$Al$_5$O$_{12}$, Lu$_3$Al$_5$O$_{12}$, YAlO$_3$, LiYF$_4$, LiLuF$_4$, BaY$_2$F$_8$, KGd(WO$_4$)$_2$, and KY(WO$_4$)$_2$ laser crystals in the 80–300," J. Appl. Phys. **98**, 103514 (2005).
30. J. Körner, V. Jambunathan, J. Hein, R. Seifert, M. Loeser, M. Siebold, U. Schramm, P. Sikocinski, A. Lucianetti, T. Mocek, and M. C. Kaluza, "Spectroscopic characterization of Yb^{3+}-doped laser materials at cryogenic temperatures," Appl. Phys. B **116**(1), 75–81 (2014).

1. Introduction

Ytterbium-doped host materials are known as excellent gain media due to the simple energy-level scheme of trivalent ytterbium (Yb^{3+}), consisting of only the $^2F_{5/2}$ excited state and the $^2F_{7/2}$ ground state, hence eliminating parasitic processes that are detrimental for amplification

and lasing, such as energy-transfer upconversion, cross-relaxation, and excited-state absorption. The monoclinic potassium rare-earth double tungstates, $KRE(WO_4)_2$ (where RE = Gd, Lu, or Y), doped with Yb^{3+} have very similar energy levels [1–4], with a characteristic total splitting of ~550 cm^{-1} within each manifold, as shown in Fig. 1. The $KRE(WO_4)_2:Yb^{3+}$ exhibit transition cross-sections significantly higher than those of $YAG:Yb^{3+}$ [5,6]. Moreover, high Yb^{3+} concentrations, up to the stoichiometric compound $KYb(WO_4)_2$, can be incorporated without significant lifetime quenching [5,7,8]. These properties are beneficial for chip-scale amplifiers and lasers, as the high transition cross-sections and high Yb^{3+} concentrations compensate for the limited interaction length and permit high gain per unit length. The large pump intensity in a waveguide structure at a wavelength of ~933 nm produces high population inversion, which enables optical amplification with a record net gain of 935 dB/cm [9] and efficient laser operation [10] at the central line of 981 nm.
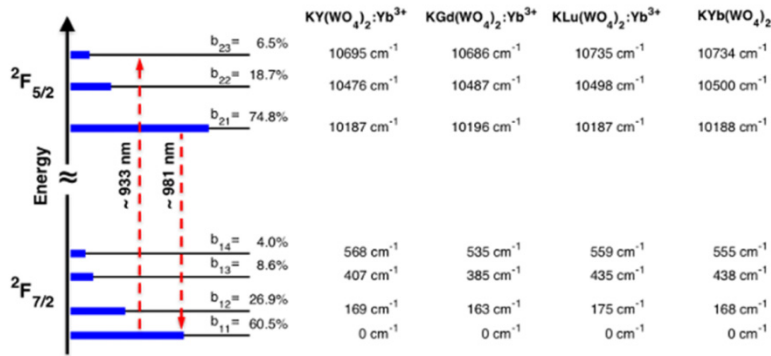

Fig. 1. Energy-level diagram of Yb^{3+} in various potassium rare-earth double tungstates [1–4]. The thick horizontal bars in blue represent the estimated fractional populations within the upper ($^2F_{5/2}$) and lower ($^2F_{7/2}$) manifolds at 300 K, calculated using the level energies of $KY(WO_4)_2:Yb^{3+}$.

Generally, two approaches can be used to grow highly Yb^{3+}-doped $KRE(WO_4)_2$ thin films. Lattice engineering can be realized by incorporating an optically inert rare-earth element to compensate the lattice mismatch caused by the high Yb^{3+} concentration [8]. Thin films produced with this method exhibit a refractive-index contrast up to ~0.02 with respect to the $KY(WO_4)_2$ substrate, making it favorable for waveguide applications. Alternatively, choosing a substrate material containing a rare-earth element with radius closest to that of Yb^{3+} [i.e., $KLu(WO_4)_2$] also allows for the successful growth of sufficiently (i.e., ~100 μm) thick and highly Yb^{3+}-doped epitaxial layers for thin-disc applications [3]. Although amplifier and laser experiments based on epitaxial layers with up to 52 at.% of Yb^{3+} have been performed [3,9], reports on the detailed investigation of the spectroscopic properties at such high Yb^{3+} concentrations are scarce [11]. Particularly, it is unclear whether the transition cross-sections remain the same given the substantial amount of Yb^{3+} ions in the sample. Furthermore, highly Yb^{3+}-doped devices may operate at elevated temperatures. In order to understand and model the operational characteristics of such amplifiers and lasers, knowledge of the dependence of the transition cross-sections on temperature is necessary. The temperature-dependent characteristics of amplifiers and lasers have been analyzed using cross-section values estimated from the temperature-dependent population of the relevant Stark level [12], however the validity of such an approximation is unclear, as it is generally known that linewidth broadening plays a role as well.

Here we investigate the temperature dependence of the absorption cross-sections in $KRE(WO_4)_2$ thin films activated by Yb^{3+}. As the reported peak-absorption cross-section of Yb^{3+} in $KRE(WO_4)_2$ at 981 nm found in the literature varies widely from 7.1×10^{-20} cm^2 to 13.3×10^{-20} cm^2 [1,13], the room-temperature absorption is carefully determined prior to the

temperature-dependent study. A key factor affecting the measurement of peak-absorption cross-sections at 981 nm, namely stray light in the measurement system, is discussed. The peak-absorption cross-sections in the thin films with Yb^{3+} concentrations exceeding 50 at.% are found to be similar to those of bulk $KRE(WO_4)_2$, suggesting that the spectroscopic properties are retained even when Yb^{3+} becomes a dominating rare-earth element in the active layer. With the aid of a fundamental theoretical analysis, we deduce that the change of the peak-absorption cross-sections at 933 nm and 981 nm with temperature is governed by the combination of two effects, the change of Stark-level population and the linewidth broadening due to intra-manifold single-phonon relaxation. Our experimental results show good agreement with the theory and confirm the strong influence of linewidth broadening on the reduction of peak-absorption cross-section values within the temperature range investigated. The theoretical analysis is applicable to other rare-earth-doped crystals and will be valuable for assessing the temperature-dependent absorption of new gain materials.

2. Sample preparation

Two samples were prepared for the experiments. The first one consists of a layer of $KYb_xGd_{1-x}(WO_4)_2$, with a nominal Yb^{3+} concentration of 57.5 at.%, grown onto commercially available 1-mm-thick, **b**-oriented $KY(WO_4)_2$ substrates (Altechna) by liquid-phase epitaxy (LPE) using a $K_2W_2O_7$ solvent at 920–925 °C [8,14]. In view of the high amount of Yb^{3+}, the lattice parameters of the epitaxial layer were engineered and optimized by co-doping with optically inert gadolinium (Gd) ions to minimize the lattice mismatch in **a** and **c** crystallographic directions. In addition, a highly temperature-stable LPE-growth system with the growth temperature controlled within ± 0.1 °C enabled us to realize a high-quality crystalline layer. Further details about the lattice engineering approach for accommodating high Yb^{3+} concentration in an epitaxial layer grown onto a $KY(WO_4)_2$ substrate can be found in [8].

The second sample is a $KYb_yLu_{1-y}(WO_4)_2$ layer with a nominal Yb^{3+} concentration of 75 at.%, grown onto a 2-mm-thick $KLu(WO_4)_2$ substrate, with the largest surface perpendicular to the **b** crystallographic direction, and cut from a single crystal that was home-grown by top-seeded solution growth (TSSG) [3]. To grow the $KYb_yLu_{1-y}(WO_4)_2$ epitaxial layer, a solution with a solute:solvent ratio 7:93 mol% was used, since it allowed us to control the growth rate of the layer [15]. The saturation temperature (T_s) was accurately determined using a $KLu(WO_4)_2$ **b**-oriented crystal seed placed in contact with the surface of the solution by adjusting to the point where neither growth nor dissolution of the seed was observed. Subsequently, the $KLu(WO_4)_2$ substrate was partially immersed into the solution at T_s by vertical dipping. Immediately after immersion, the temperature of the solution was decreased by 3 K below T_s and the epitaxial growth process was undertaken at this temperature for 3 hours. Finally, the substrate was removed from the solution and the furnace was cooled to room temperature at 15 K h^{-1}, thus preventing cracking of the structures by thermal shock.

The Yb^{3+} concentrations of both samples were determined with an Energy Dispersive X-ray (EDX) module attached to a Scanning Electron Microscope (Zeiss Merlin HR-SEM), resulting in $x = 0.57 ± 0.03$ at.% for the $KYb_xGd_{1-x}(WO_4)_2$ layer and $y = 0.76 ± 0.03$ at.% for the $KYb_yLu_{1-y}(WO_4)_2$ layer. We will refer to these two samples as $KYb_{0.57}Gd_{0.43}(WO_4)_2$ and $KYb_{0.76}Lu_{0.24}(WO_4)_2$, respectively, hereafter. The rear surface of each sample was lapped and polished to remove the excess growth layer, whereas their respective front surface was lapped and polished parallel to the substrate. The final thicknesses of the $KYb_{0.57}Gd_{0.43}(WO_4)_2$ and the $KYb_{0.76}Lu_{0.24}(WO_4)_2$ epi-layers were measured with a Dektak profilometer and found to be ~32 μm and ~124 μm, respectively.

3. Absorption measurements on films with high ytterbium concentration

3.1 Measurement setups

A dual-beam spectrophotometer (Shimadzu UV1800) with a spectral bandwidth of 1 nm is used together with a near-infrared (NIR) polarizer with >400:1 extinction ratio (Thorlabs LPNIRE100-B) to determine the absorbance of both samples, as shown in Fig. 2(a). Wavelength scans from 900 nm to 1050 nm with data acquisition in 0.1 nm steps are performed to determine the absorption due to Yb^{3+} ions. As the epitaxial layers were grown along the N_p direction, absorption spectra with $E\|N_m$ and $E\|N_g$ polarization can be measured. We limit our study to the absorption polarized to $E\|N_m$, because this polarization exhibits the highest transition cross-sections and, therefore, is more commonly used for amplifier and laser experiments than the $E\|N_g$ polarization. A series of measurements is performed while the polarizer is rotated by ~180° in steps to determine the sample orientation for absorption polarized to $E\|N_m$. The absorption spectrum for each angle step is corrected for the spectral response of the polarizer at the same angle as well as the Fresnel reflections of the sample. The $E\|N_m$ polarization is identified by the angle which produces the highest corrected absorption at the central absorption line near 981 nm wavelength. This peak absorption value follows a sinusoidal-like trend as the polarization angle is changed. The temperature-dependent absorption measurement is performed on $KYb_{0.57}Gd_{0.43}(WO_4)_2$ using this setup. A copper sample holder in contact with a Peltier element, as shown on the right of Fig. 2(a), is used. The temperature of the sample is regulated using a thermoelectric temperature controller (Melcor MTTC1410).
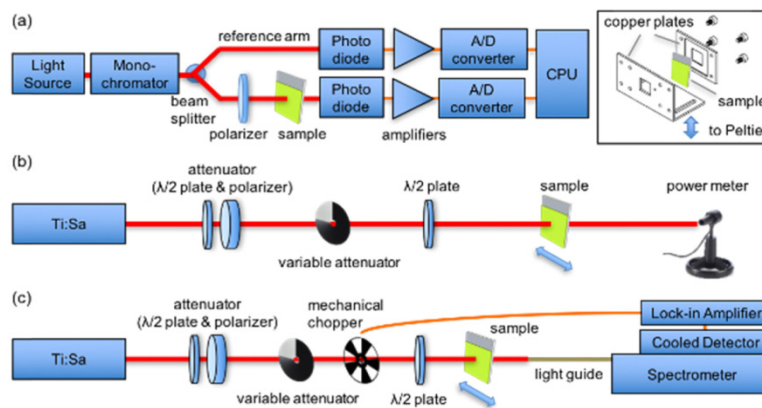

Fig. 2. Schematic diagrams of (a) the commercial dual-beam spectrophotometer with a polarizer, (b) the free-space measurement setup with optical detection by a power meter, and (c) the free-space measurement setup with optical detection by a cooled detector attached to a spectrometer. The sample holder used for the temperature-dependent study is shown at the right of (a).

Figure 2(b) shows a free-space setup with a Ti:Sapphire laser (Spectra-Physics 3900S, linewidth <40 GHz) used for the measurement of the $KYb_{0.76}Lu_{0.24}(WO_4)_2$ sample with a high total absorption of ~35 dB at 981 nm wavelength. The intensity of the beam is attenuated to <0.5 W/cm^2 over the entire measured wavelength range to ensure that it is much lower than the saturation intensity of 5.4 kW/cm^2 [5] at 981 nm. A broadband half-wave plate is used to rotate the polarization of the light source. In order to identify the $E\|N_m$ axis the transmission at 981 nm wavelength is measured and the half-wave plate is rotated until a minimal power is transmitted through the sample. A silicon detector (Coherent OP-2 VIS) with a specified detection range of ~50 dB at 1000 nm wavelength is used to measure the transmitted optical power as the sample is positioned within/out of the beam path. The probe wavelength is tuned manually with tuning steps of ≤5 nm. The tuning step is gradually reduced to 1 nm and then

0.25 nm near the absorption peaks at 933 nm and 981 nm, respectively, to minimize the data acquisition time while ensuring that the absorption peaks are well resolved. For each wavelength step, three data points are recorded and an averaged absorption value is deduced. Figure 2(c) shows the variation of the free-space setup to further minimize the influence of stray light. After passing through the sample, the probe beam is passed through a spectrometer (Jobin Yvon iHR550). The detection wavelength is tuned to the probe-beam wavelength, hence any residual luminescence from the Ti:Sapphire laser crystal at other wavelengths is effectively discriminated from detection. A cooled detector and lock-in amplification are used to increase the signal-to-noise ratio.

3.2 Absorption measurements

Figure 3(a) shows the absorption spectra of $KYb_{0.76}Lu_{0.24}(WO_4)_2$ measured with the different setups for the polarization $E\|N_m$. In the case of the spectrophotometer, the maximum measured total absorbance of the sample and polarizer is merely ~2.6 optical density (O.D.), although the measurement instrument has a specification of 4 O.D. Such an effect is known for measurements on samples with high absorbance and is due to the stray light from the dispersive grating element which scatters a small amount of light at other wavelengths [16]. As the spectrophotometer is tuned to 981 nm, the signal is heavily attenuated, whereas the stray light at other wavelengths experiences little or no absorption. Hence, the total intensity recorded by the detector at the peak is higher than the true transmitted intensity at 981 nm and the system produces a lower absorption reading.
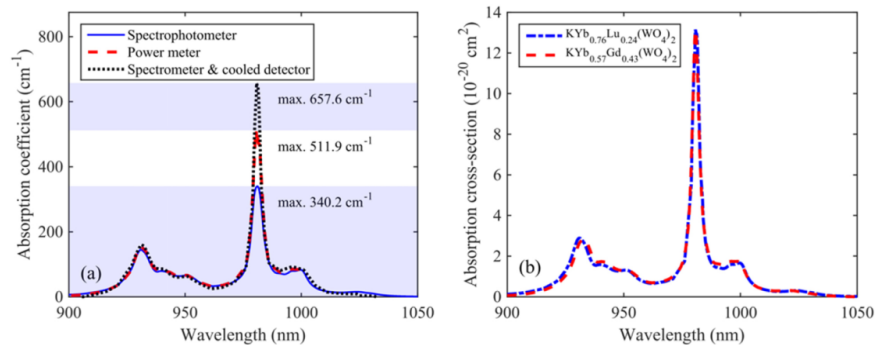

Fig. 3. (a) Absorption spectra polarized to $E\|N_m$ for the $KYb_{0.76}Lu_{0.24}(WO_4)_2$ sample with high total absorbance measured using the spectrophotometer (blue solid curve), free-space setup with power meter (red dashed curve), and free-space setup with cooled detector attached to a spectrometer (black dotted curve). (b) Calculated effective absorption cross-section in the $KYb_{0.76}Lu_{0.24}(WO_4)_2$ and $KYb_{0.57}Gd_{0.43}(WO_4)_2$ samples.

The stray-light problem is circumvented by use of higher signal power or a light source with better signal-to-noise ratio. Hence, the free-space setup displayed in Fig. 2(b) is used to repeat the measurement in $KYb_{0.76}Lu_{0.24}(WO_4)_2$. The result, displayed in Fig. 3(a) as the dashed curve, shows a better-resolved absorption peak with a maximum absorption coefficient of 512 cm^{-1}. Nevertheless, when the probe beam is tuned to 981 nm, the wavelength spectrum collected after the sample still reveals some detectable residual NIR luminescence (~700–850 nm) from the Ti:Sapphire laser crystal. In order to further suppress the stray light, the probe beam is sent to the spectrometer equipped with a cooled detector, as shown in Fig. 2(c). Using this setup, the peak-absorption coefficient is well resolved and approaches 658 cm^{-1} [see Fig. 3(a), dotted curve], which is nearly two times the initial value obtained with the spectrophotometer. Applying the calculation method described in [16], the respective amount of stray light in the spectrophotometer, the free-space setup with power meter, and the free-space setup with spectrometer and cooled detector are approximated as ~0.25%, ~0.15%, and <0.002% of the probe-beam intensity at 981 nm.

The effective absorption cross-section, σ_{abs}, is calculated from the measured absorption coefficient, α, and the known Yb^{3+} concentration, N_{Yb},

$$\sigma_{abs}(\lambda, T) = \alpha(\lambda, T)/N_{Yb} . \qquad (1)$$

Figure 3(b) depicts the calculated effective absorption cross-section of the $KYb_{0.76}Lu_{0.24}(WO_4)_2$ layer, with N_{Yb} of 5.0×10^{21} cm^{-3}. The absorption data are taken from Fig. 3(a), using the spectrophotometer measurement result in the low-absorption range and the measurement results from the free-space setup with spectrometer and cooled detector at the peak-absorption region (970–985 nm) to retain data with good signal-to-noise ratio over the entire spectrum. Figure 3(b) also shows the absorption cross-section of the $KYb_{0.57}Gd_{0.43}(WO_4)_2$ layer at $E\|N_m$, calculated from N_{Yb} of 3.8×10^{21} cm^{-3} and using the absorption spectrum measured with the spectrophotometer setup. As the thickness and the Yb^{3+} concentration of the $KYb_{0.57}Gd_{0.43}(WO_4)_2$ sample are only ~1/4 and ~3/4 of the $KYb_{0.76}Lu_{0.24}(WO_4)_2$ sample, respectively, the corresponding total absorption is much lower. Therefore, the stray light is not significant at the absorption peak near 981 nm and it is sufficient to use only the spectrophotometer setup for the $KYb_{0.57}Gd_{0.43}(WO_4)_2$ sample.

Both absorption spectra in Fig. 3(b) are found to be very similar to those of stoichiometric $KYb(WO_4)_2$ [5], $KGd(WO_4)_2$:(1 at.%)Yb^{3+} [2], and $KLu(WO_4)_2$:(0.7 at.%)Yb^{3+} [3]. Particularly, they are in excellent agreement with that of $KY(WO_4)_2$:(~5 at.%)Yb^{3+} [1], especially at the peak absorption value at 981 nm. The fact that no abnormality is observed in the absorption of the epitaxial layers shows that they are of high quality and the small lattice mismatch does not perturb the crystal field. This is in contrast to other Yb^{3+} hosts, such as LuAG and YAG, where color centers are apparent on as-grown samples especially at higher Yb^{3+} concentration [17,18]. The calculated peak cross-section based on our measurements is 1.32×10^{-19} cm^2 for $KYb_{0.76}Lu_{0.24}(WO_4)_2$ and 1.31×10^{-19} cm^2 for $KYb_{0.57}Gd_{0.43}(WO_4)_2$. This small difference is within the measurement errors of the experimental setups. Table 1 compares the calculated peak-absorption cross-section values in this work to those of bulk $KRE(WO_4)_2$:Yb^{3+}. The values determined in this work favorably match the value of 1.33×10^{-19} cm^2 in $KY(WO_4)_2$:(~5 at.%)Yb^{3+} [1], though a lower cross-section value of 1.17×10^{-19} cm^2 had also been reported for the same material [20]. On the other hand, the $KYb(WO_4)_2$ [5,19], $KGd(WO_4)_2$:Yb^{3+} [1] and $KLu(WO_4)_2$:Yb^{3+} [21] are reported to exhibit peak cross-section value of ~1.2×10^{-19} cm^2. The slight differences among the reported peak cross-section values may be attributed to the spectral resolution of the different measurement systems and/or the value of doping concentration used for the calculation of cross-sections. Based on the results in Fig. 3(b) as well as the comparison of the values in Table 1, it is reasoned that the spectroscopic properties of the highly Yb^{3+}-doped thin films are comparable to bulk potassium rare-earth double tungstates with low Yb^{3+} concentration and stoichiometric potassium ytterbium double tungstate.

Table 1. Comparison of peak effective absorption cross-section values of Yb^{3+}-doped potassium rare-earth double tungstates near 981 nm.

Material composition	Yb^{3+} concentration [10^{20} cm^{-3}]	Bulk / Epitaxial layer	Peak cross-section [10^{-19} cm^2]	Reference
$KY(WO_4)_2$:Yb^{3+}	3	Bulk	1.33	Kuleshov et al. [1]
$KGd(WO_4)_2$:Yb^{3+}	2.2	Bulk	1.20	Kuleshov et al. [1]
$KYb(WO_4)_2$	64	Bulk	1.17	Pujol et al. [19]
$KY(WO_4)_2$:Yb^{3+}	0.709	Bulk	1.17	Mateos et al. [20]
$KLu(WO_4)_2$:Yb^{3+}	0.45	Bulk	1.18	Mateos et al. [21]
$KYb_{0.76}Lu_{0.24}(WO_4)_2$ / $KLu(WO_4)_2$	50	Epitaxial	1.32	This work
$KYb_{0.57}Gd_{0.43}(WO_4)_2$ / $KY(WO_4)_2$	38	Epitaxial	1.31	This work

4. Temperature dependence of cross-sections

4.1 Absorption spectra and decomposition of absorption peaks

The σ_{abs} in $KYb_{0.57}Gd_{0.43}(WO_4)_2$ is determined from the measured absorption spectrum as a function of temperature, which is varied in controlled steps of 10 °C between 20 and 170 °C. The maximum temperature is limited by the Peltier element used in the setup. Figure 4(a) shows the evolution of σ_{abs} versus temperature. As the temperature is increased, the central absorption line near 981 nm reduces rapidly. The wavelength corresponding to the peak is slightly blue-shifted from 980.8 nm to 980.5 nm. A similar, but less drastic, reduction of absorption is also noted at the peak near 933 nm. However, the corresponding peak wavelength for this transition is shifted more from 932.9 nm at 20 °C to 931.7 nm at 170 °C.
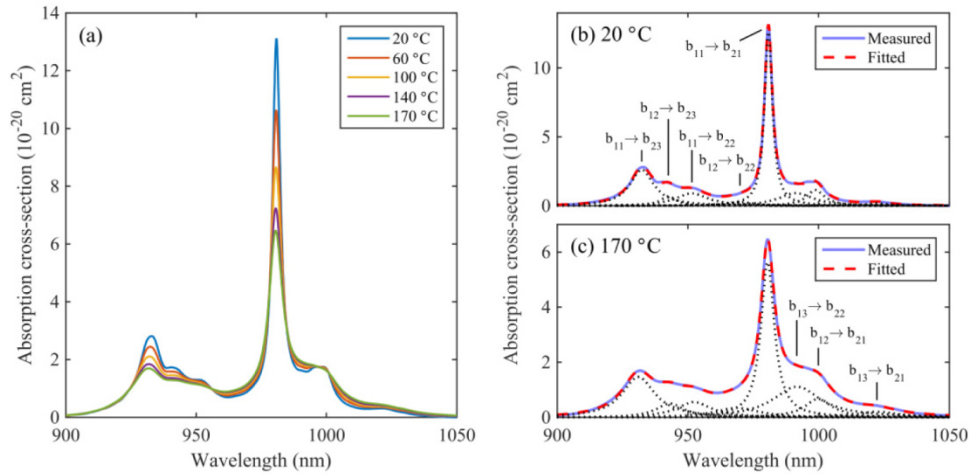

Fig. 4. (a) Temperature dependence of the absorption cross-section of the $KYb_{0.57}Gd_{0.43}(WO_4)_2$ sample. Multi-peak fitted absorption cross-section at (b) 20 °C and (c) 170 °C. The dotted lines show the decomposed peaks corresponding to different inter-Stark transitions. The eight transitions wavelengths are labeled and positioned near to one of the curves where its decomposed peak is more pronounced.

The temperature dependence of the peak σ_{abs} at 933 nm and 981 nm shown in Fig. 4(a) is further investigated by considering peak decomposition using multiple peaks fitting on the measured spectra with

$$\sigma_{abs}(\lambda,T) = \sum b_{1N}(T)\sigma_{atom}(\lambda,T),\qquad(2)$$

where b_{1N} is the fraction of total population of the N-th Stark level within the ground-state manifold (where $N = 1, 2, 3,$ or 4, see Fig. 1) relevant to the absorption transition, which can be estimated with the difference of energy with respect to the lowest Stark level, $E_{1N} - E_{11}$, the Boltzmann constant, k_B, and the temperature, T, using the following expression

$$b_{1N}(T) = \frac{\exp\left[-\left(E_{1N} - E_{11}\right)/k_B T\right]}{\sum\limits_{j=1}^{4}\exp\left[-\left(E_{1j} - E_{11}\right)/k_B T\right]}.\qquad(3)$$

σ_{atom} represents the atomic transition cross-section, which can be modeled in the frequency domain using the expression [22,23]

$$\sigma_{atom}(\nu) = S\,\tilde{\gamma}(\nu),\qquad(4)$$

where v is the frequency. The term $\tilde{\gamma}(v)$ represents the spectral line-shape function. Considering the crystalline nature of the material, homogeneous broadening would dominate and $\tilde{\gamma}(v)$ is described by the Lorentzian function

$$\tilde{\gamma}(v) = \frac{1}{\pi} \frac{\Delta v/2}{(v-v_0)^2 + (\Delta v/2)^2} \quad \text{with} \quad \int \tilde{\gamma}(v)\, dv = 1, \tag{5}$$

where v_0 is the center frequency and Δv is the full width at half maximum (FWHM). Δv strongly depends on temperature. Also small frequency shifts of v_0 with increasing T are observed.

$$S = \int \sigma_{atom}(v)\, dv = \int \sigma_{atom}(v_0) \frac{\pi}{2} \Delta v\, \tilde{\gamma}(v)\, dv = \sigma_{atom}(v_0) \frac{\pi}{2} \Delta v \tag{6}$$

is the integral transition cross-section [23], in units of (m^2/s), which is independent of frequency and also considered independent of temperature, because Δv and $\sigma_{atom}(v_0)$ depend in opposite ways on temperature [23].

The multiple peak fitting is performed using a data analysis program (Origin 9.1). Representative fitted absorption curves measured at 20 °C and 170 °C are depicted in Figs. 4(b) and 4(c). The 8 out of 12 total possible Stark-level transitions used for the fitting are also labelled in the figure. In the event of overlapping transitions, we consider the transition that involves lower Stark levels to be more relevant, assuming that both transition strengths are similar. For instance, the $b_{13} \rightarrow b_{23}$ transition (~970 nm) overlaps with the more prominent $b_{12} \rightarrow b_{22}$ transition, therefore it is not treated as an independent peak. This also applies to the $b_{14} \rightarrow b_{23}$ (~982 nm) and $b_{14} \rightarrow b_{22}$ (~1005 nm) transitions, which are overshadowed by the $b_{11} \rightarrow b_{21}$ and $b_{12} \rightarrow b_{21}$ transitions, respectively, due to much lower fractional population of the b_{14} Stark level. The remaining $b_{14} \rightarrow b_{21}$ transition is not considered in the fitting, because the measured absorption is less apparent compared to other peaks. Besides, excluding this transition in the fitting has negligible impact on the following studies, because the corresponding transition wavelength of ~1040 nm is far from the 933 nm and 981 nm wavelengths. The peak absorption is well described by the Lorentzian shape even at 170 °C, thereby confirming the dominance of homogeneous broadening over the measurement range.

4.2 Temperature dependence of major absorption lines

From Fig. 4(c), it is observed that the absorption peaks at 933 nm and 981 nm dominate even at 170 °C. For both cases, the magnitudes of their respective neighboring transitions are relatively weak. Assuming that the influence of neighboring transitions is negligible and the integral transition cross-section is independent of temperature, the temperature dependence of these major absorption peaks can be approximated from Eqs. (2)–(6) using only a single-peak representation,

$$\sigma_{abs}(T) \approx b_{11}(T)\, S\, \frac{2}{\pi\, \Delta v(T)} \tag{7}$$

or

$$\sigma_{abs}(T) \propto \frac{b_{11}(T)}{\Delta v(T)}. \tag{8}$$

Hence, once the effective absorption cross-section at a reference temperature, T_0 (e.g. room temperature), is known, the effective absorption cross-section at an arbitrary temperature, T, can be approximated by

$$\sigma_{abs}(T) = \sigma_{abs}(T_0)\frac{b_{11}(T)}{b_{11}(T_0)}\frac{\Delta\nu(T_0)}{\Delta\nu(T)}. \qquad (9)$$

Equation (9) signifies that the peak-absorption cross-section changes with temperature according to the temperature dependence of i) the Boltzmann factor of the starting Stark level and ii) the absorption linewidth. Figure 5(a) shows the value of b_{11} at various temperatures, calculated based on the level energies of $KY(WO_4)_2:Yb^{3+}$. The values deviate by less than 2.5% if any of the other sets of level energies shown in Fig. 1 is chosen. When the temperature increases from 20 °C to 170 °C, the value of b_{11} is reduced by ~18%. Figure 5(b) displays the extracted FWHM of the decomposed absorption peaks near 933 nm and 981 nm, indicating that their FWHM at the highest temperature is ~1.37 and ~1.72 times broader at 170 °C than at 20 °C, respectively. The corresponding ratio of $\Delta\nu(20\ °C)/\Delta\nu(170\ °C)$ is ~0.73 and ~0.58 for the respective transitions at 933 nm and 981 nm.

The change of the peak-absorption cross-sections at elevated temperatures with respect to 20 °C, $\sigma_{abs}(T)/\sigma_{abs}(20\ °C)$, is shown in Fig. 5(c). A reduction by ~40% and ~52% for the transitions near 933 nm and 981 nm, respectively, occurs. The result from the simple model of Eq. (9) is in good agreement with the measured reduction of peak magnitudes, showing that the origin of the reduction of peak-absorption cross-section with temperature is a combination of the change in the population of the starting Stark level with temperature and the widening of the transition linewidth with temperature. In the high-temperature range, the simple model starts to deviate from the measurement points and the contributions from adjacent peaks need to be taken into account.
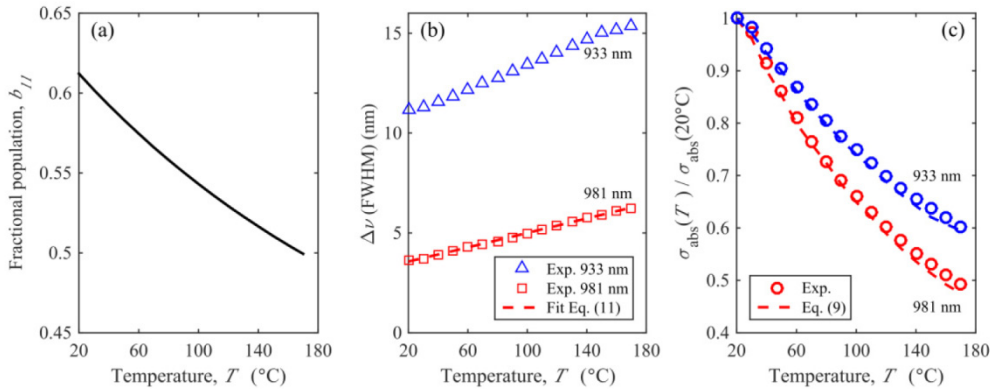

Fig. 5. Spectroscopic data as a function of temperature: (a) calculated fractional population b_{11}, (b) extracted $\Delta\nu$ (FWHM) of the absorption peaks near 933 nm and 981 nm and the fitted curve using Eq. (11), and (c) relative change of peak-absorption cross-section σ_{abs} of the transitions near 933 nm and 981 nm in $KYb_{0.57}Gd_{0.43}(WO_4)_2$ and the calculated curves using Eq. (9).

4.3 Temperature dependence of emission spectra and lifetime

The temperature-dependent emission cross-sections σ_{em} were calculated from the corresponding absorption spectra of Fig. 4(a) using the reciprocity method [24],

$$\sigma_{em}(\lambda, T) = \sigma_{abs}(\lambda, T)\frac{Z_g}{Z_e}\exp\left(\frac{E_{zl} - hc/\lambda}{kT}\right), \quad Z_i = \sum_i d_i e^{-\frac{E_i}{kT}}, \qquad (10)$$

where h is the Planck constant, k is the Boltzmann constant, T is the temperature, E_{zl} is the energy of the zero-phonon line, and the calculated partition functions at 20 °C are $Z_g = 3.2670$ for the ground state and $Z_e = 2.6495$ for the excited state. The calculated emission spectra for different temperatures are displayed in Fig. 6(a) and the temperature dependence of the

effective emission and absorption cross-sections at the peak wavelengths of 981 nm and 933 nm is compared with each other in Fig. 6(b). At 981 nm the Boltzmann distribution of the emitting level contributes to a decrease of the effective emission cross-section with increasing temperature, thereby adding up with the effect of linewidth broadening, resulting in a temperature dependence similar to that of the effective absorption cross-section. In contrast, at 933 nm the Boltzmann distribution of the emitting level contributes to an increase of the effective emission cross-section with increasing temperature, thereby counter-acting the effect of linewidth broadening, resulting in a temperature dependence that differs from that of the effective absorption cross-section.
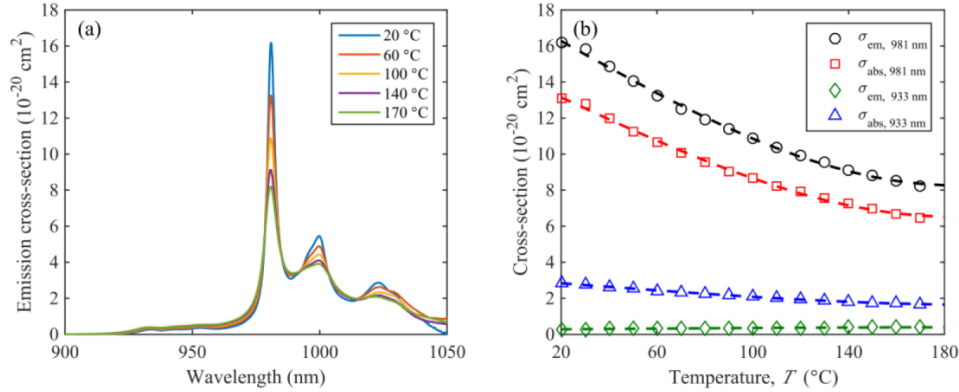

Fig. 6. (a) Temperature dependence of the effective emission cross-section of the $KYb_{0.57}Gd_{0.43}(WO_4)_2$ sample as calculated with the reciprocity method from the spectra of Fig. 4(a). (b) Comparison of temperature dependence of effective emission and absorption peak cross-sections at 981 nm and 933 nm. The dashed lines are a guide for the eye.

The luminescence lifetime at wavelengths longer than 1000 nm is measured in the $KYb_{0.57}Gd_{0.43}(WO_4)_2$ sample with chopped quasi-cw excitation at 981 nm using the pinhole method [25], while the temperature is varied from 20 °C to 160 °C in steps of 20 °C. No significant temperature dependence is observed. The mean value of all data points is 230 μs and deviations of individual data points from the mean value are within ± 5%.

5. Discussion

5.1 Origin of linewidth broadening

Given the substantial influence of linewidth broadening on the temperature dependence of peak-absorption cross-sections, understanding the origin of linewidth broadening may help to generate a simple model that can describe the temperature dependence over a wide range of temperatures. The measured linewidth Δv is caused by intra-manifold transitions due to electron-phonon coupling on the fs time scale [23], which establishes the Boltzmann distribution. Considering a single-phonon contribution to the homogeneous broadening, i.e., the transition is accompanied by the absorption/emission of one phonon, a simplified expression can be derived from the detailed calculation of the electron-phonon interaction for non-adiabatic systems [26,27],

$$\Delta v(T) \propto \left[\exp\left(\hbar\omega/k_B T\right)-1\right]^{-1}, \tag{11}$$

where $\hbar\omega$ is the energy of the phonon involved in the transition. This is the Bose-Einstein statistics applied to occupation of a phonon mode as a function of temperature.

Applying Eq. (11) to the extracted linewidth at 981 nm given in Fig. 5(b), a least-squares fit provides $\hbar\omega = 164.3 \pm 12$ cm^{-1}, which corresponds to the energy gap between E_{12} and E_{11}.

The obtained $\hbar\omega$ is reasonable, because the sum of fractional populations of these two Stark levels is ~87.4% at room temperature.

5.2 Extension of study to situations of cryogenic cooling

Amplifiers and lasers operating under intense optical pumping may experience significant thermal build up. Therefore, efficient heat removal is typically important for a proper performance of these devices. The findings in Figs. 4 and 5 are valuable for the investigation of devices operation without thermal management, passively cooled, or actively cooled via a Peltier element. Cryogenic cooling provides an option to further exploit the potential of the active material, in which a substantial increase in transition cross-sections, a reduction of population density in the lower laser level, and improvement of thermo-optical properties can be achieved [28–30]. With the insight on the linewidth characteristics from Eq. (11), the peak-absorption cross-section at cooled temperatures can be estimated, assuming that Eq. (11) is valid over the temperature range under consideration.

Figure 7 shows the contribution of the linewidth and the fractional population to the change of peak-absorption cross-section at 981 nm from room temperature down to 77 K. The fractional population increases from ~61% to ~96%, whereas the FWHM reduces from ~3.5 nm to ~0.2 nm, each contributing a 1.6 × and 16 × enhancement factor to the absorption cross-section. The transition cross-section at 981 nm is expected to increase by a factor of 25 at 77 K and it is strongly influenced by the actual linewidth at the given temperature.
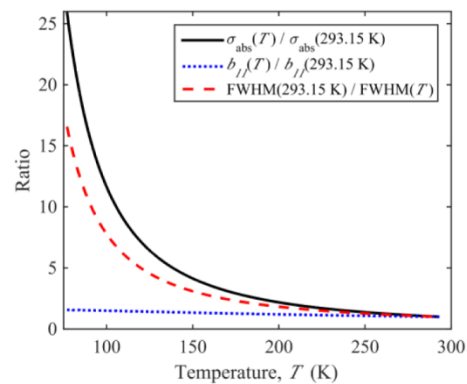

Fig. 7. Calculated ratio of effective peak-absorption cross section, σ_{abs}, at 981 nm, fractional population of lowest Stark level, b_{11}, of the ground state and the FWHM $\Delta\nu$ as a function of cooling temperature, T.

6. Conclusion

The measured absorption data collected from highly Yb^{3+}-doped potassium rare-earth double tungstate thin films have been presented. Care has been taken to reduce stray light in order to resolve the absorption peak. The calculated peak-absorption cross-sections from two thin films with >50 at.% of Yb^{3+} are found to be comparable to those of reported bulk materials. Temperature-dependent absorption measurements revealed a strong dependence of the major absorption peaks at 933 nm and 981 nm on temperature. With the aid of a simple model, the reduction of peak-absorption cross-section can be explained by two effects, the reduced fractional population of the relevant Stark level and the linewidth broadening. The same model can be readily adapted on other rare-earth-doped crystals to evaluate the temperature-dependency of the respective absorption at the pump and signal wavelengths. Further investigation on the magnitude of the extracted linewidths reveals that intra-manifold relaxation within the two lowest Stark levels plays a role in the broadening phenomenon for the central absorption line at 981 nm. The effective emission cross-sections versus temperature have been calculated. Luminescence-decay measurements show no significant

dependence of the luminescence lifetime on temperature. The reported results are not only useful for the understanding of amplifiers and lasers operating above room temperature, but also provide insight on the potential of enhanced absorption at 981 nm for the design of cryogenically cooled devices.